Monthly Notices
of the
ROYAL ASTRONOMICAL SOCIETY

Mon. Not. R. Astron. Soc. **422,** 1098–1108 (2012) doi:10.1111/j.1365-2966.2012.20683.x

The molecular emissions and the infall motion in the high-mass young stellar object G8.68−0.37

Zhiyuan Ren,[1⋆] Yuefang Wu,[1⋆] Ming Zhu,[2] Tie Liu,[1] Ruisheng Peng,[3] Shengli Qin[4] and Lixin Li[1,5]

[1]*Department of Astronomy, Peking University, 100871 Beijing, People's Republic of China*
[2]*National Astronomical Observatory of China, 20A Datun Road, Chaoyang District, Beijing, People's Republic of China*
[3]*Caltech Submillimeter Observatory, 111 Nowelo St., Hilo, HI 96720, USA*
[4]*I. Physikalisches Institut, Universität zu Köln, Zulpicher Str. 77, 50937 Köln, Germany*
[5]*The Kavli Institute for Astronomy and Astrophysics, Peking University, Yi He Yuan Lu 5, Hai Dian Qu, Beijing 100871, People's Republic of China*

Accepted 2012 February 2. Received 2012 February 1; in original form 2010 December 22

ABSTRACT

We present a multi-wavelength observational study towards the high-mass young stellar object G8.68−0.37. A single massive gas-and-dust core is observed in the (sub)millimetre continuum and molecular line emissions. We fitted the spectral energy distribution (SED) from the dust continuum emission. The best-fitting SED suggests the presence of two components with temperature of $T_{\rm d} = 20$ and 120 K, respectively. The core has a total mass of up to $1.5 \times 10^3\,{\rm M}_\odot$ and a bolometric luminosity of $2.3 \times 10^4\,{\rm L}_\odot$. Both the mass and luminosity are dominated by the cold component ($T_{\rm d} = 20$ K). The molecular lines of $C^{18}O$, $C^{34}S$, DCN and thermally excited CH_3OH are detected in this core. Prominent infall signatures are observed in the ^{12}CO (1 − 0) and (2 − 1). We estimated an infall velocity of 0.45 km s^{-1} and a mass infall rate of $7 \times 10^{-4}\,{\rm M}_\odot\ {\rm yr}^{-1}$. From the molecular lines, we have found a high DCN-to-HCN abundance ratio of 0.07. The overabundant DCN may originate from a significant deuteration in the previous cold pre-protostellar phase. And the DCN should now be rapidly sublimated from the grain mantles to maintain the overabundance in the gas phase.

Key words: stars: formation – stars: pre-main sequence – ISM: individual object: G8.68−0.37 – ISM: kinematics and dynamics – ISM: molecules.

1 INTRODUCTION

Gravitational infall or core collapse can take place in high-mass young stellar objects (YSOs) at early stages and continue all the way to the stage of Ultra Compact (UC) H II regions (Keto 2003; Sollins, Ho & Paul 2005). As shown by theoretical works (Jijina & Adams 1996; Yorke & Sonnhalter 2002; Gong & Ostrike 2009, etc.), the infall motion is critical for initiating the high-mass star formation and maintaining the accretion flow to feed the stellar mass during the subsequent evolutionary stages. However, further observations are still needed to better constrain the physical properties of the infall, including its spatial distribution, mass infall rate, chemical effect, and to understand its relation with other dynamical processes, including outflow, disc accretion and core fragmentation. In recent decades, extensive spectroscopic surveys (e.g. Wu & Evans 2003; Fuller, Williams & Sridharan 2005; Purcell et al. 2006; Wyrowski et al. 2006; Wu et al. 2007) have been performed towards the potential high-mass YSOs throughout the Milky Way. As a result, many infall candidates have been identified based on their spectral signatures. These sources can serve as good candidates to study the massive star birth and gas dynamics in the molecular cores. In the mean time, strong outflows are also widely detected towards those massive cores (e.g. Beuther et al. 2002; Wu et al. 2004; Zhang et al. 2007). The infall and outflow motions should be closely related and interacting with each other throughout the star formation history.

G8.68−0.37 (G8.68 hereafter) is a young high-mass star-forming region at a distance of 4.5 kpc (Mueller et al. 2002). In this region, compact multiple gas-and-dust clumps have been discovered by Longmore et al. (2011, L11 here after). The dusty core is associated with strong 6.7 GHz methanol masers (Walsh et al. 1998), but has no radio continuum emission, indicating that high-mass stars are already formed, but have not yet ionized the surrounding gas. L11 also detected a bi-polar outflow in CO (2 − 1). The outflow may be responsible for the shock interaction traced by the extended 4.5 μm emission (fig. 2 therein). In the mean time, the observation in HCO^+ (1 − 0) suggests a plausible infall motion (Purcell et al. 2006) which should be examined quantitatively. To improve the understanding in physical and chemical properties of this source, we performed

⋆E-mail: rzy,ywu@pku.edu.cn

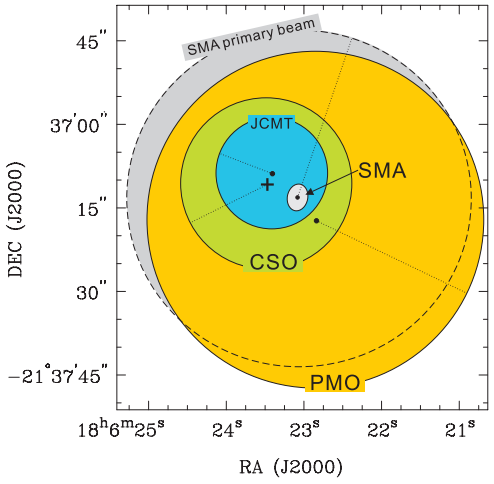

Figure 1. The beam size and pointing centre of each instrument. The cross symbol marks the centre of the 1.3 mm dust core (Fig. 4) which is coincident with the CSO pointing centre. The white ellipse is the synthesized beam of the SMA in the 2008 observation, and the grey-filled circle is the primary beam. The JCMT beam size is for the frequency of 289 GHz.

a multi-wavelength study using both the single-dish antennas and the interferometers. The next section introduces the observations and data reduction, Section 3 presents the general observational results. Section 4 describes the dust continuum and molecular line emissions, wherein the infall signature is specifically described in Section 4.3. A summary is given in Section 5.

2 OBSERVATIONS AND DATA REDUCTION

2.1 The single dishes

In Fig. 1, we show the central positions and the beam sizes of all the observations. We observed G8.68 using three different single-dish telescopes. In 2005, we observed HCN (3−2) and $H^{13}CO^+$ (3 − 2) from the James Clerk Maxwell Telescope[1] (JCMT). The pointing centre was adopted to be the coordinate of the strongest methanol maser (Walsh et al. 1998, with a position accuracy of 1.8 arcsec), which is close to the continuum emission peak of L11 (cross in Fig. 1). The mapping step is 10 arcsec (corresponding to 1/2 beam size), as shown in Fig. 2(b).

In 2009 November, we observed $J = 1 - 0$ line of ^{12}CO, ^{13}CO and C^{18}O using the 13.7-m telescope at the Purple Mountain Observatory[2] (PMO). The PMO observation contains a grid mapping with a coverage of several arcminutes over the region of G8.68. In this paper, we only use the spectra at one point which is closest to the continuum peak as shown in Fig. 1. The PMO beam is much larger than the Caltech Submillimeter Observatory (CSO) and JCMT, and is significantly deviated from the continuum peak. Nevertheless, the beam covers the emission regions of the continuum and molecular lines well. The data can thus be used to trace the gas motion on a larger scale near the core.

In 2011 May, the $J = 2 - 1$ lines of the three CO isotopologues were observed from the 10-m telescope at the CSO[3]. The ^{12}CO (2 − 1) is observed at five symmetric points around the continuum peak with an offset of ±23 arcsec in the Right ascension (RA) and declination (Dec.) directions. Their positions are shown in Fig. 2(a). All the single-dish spectra are discussed in detail in Section 3.2.2.

In Table 1, we present the basic observational parameters and weather conditions for the three instruments. In Table 2, we show the more specific observational parameters for the molecular lines. All the observations were performed in good weather conditions, with pointing accuracies better than 5 arcsec. GILDAS software package[4] was used for the data reduction and image plot.

To measure the flux densities at different wavelengths, we also retrieved the *Spitzer* archival images at four IRAC bands from the GLIMPSE Survey,[5] and the 24 and 70 μm images from MIPSGAL,[6] and JCMT/Submillimetre Common-User Bolometer Array (JCMT/SCUBA) images at 450 and 850 μm bands, which are available at the Canadian Astronomy Data Center (CADC) repository of the SCUBA Legacy Fundamental Object Catalogue.[7]

2.2 The Submillimeter Array

The Submillimeter Array[8] (SMA) observations towards G8.68 are taken from the released SMA data archive. The observations are made in three epochs in the years 2007, 2008 and 2009, respectively. The observational parameters, including the calibration sources for each epoch, are presented in Table 3. In all three epochs the compact array was used and the phase tracking centre is RA (J2000) = $18^h06^m23.23^s$, Dec. (J2000) = $-21°37'14.19''$. The three observations have similar beam sizes for the synthesized and primary beams. In Fig. 1, we only show the beams of the 2008 observation in order to have a clear appearance. The observed gas-and-dust structures (Fig. 4) turn out to be smaller than the SMA primary beam. Thus the beam-edge weakening is not significant. The calibration and imaging were performed in Miriad[1]. The absolute flux level has an uncertainty of ∼15 per cent. The continuum emission was subtracted from the line-free channels in each sideband. The gain solution is self-calibrated for the continuum image and then exported to the spectral line data.

We note that among the SMA data, the 2008 observation has the longest on-source integration time, hence the lowest noise level. In addition, in 2008 all eight antennas of the SMA were at work, while the 2007 observation (280 GHz) only employed seven antennas. As a result, despite its higher frequency, the 2007 data have a lower angular resolution than the 2008 data (as indicated by their synthesized beam sizes in Table 3). We therefore used the 2008 data (frequency centred at 225 GHz or 1.3 mm) to analyse the dust continuum emission. The continuum was averaged from the line-free channels and then subtracted from the side-band spectrum. The continuum data of the two sidebands were averaged on the (u,v) plane and then converted to the image domain. After cleaning and self-calibration, the 1.3 mm continuum image has an rms noise level (1σ) of 3.6 mJy beam^{-1} (corresponding to a brightness temperature of $T_b = 0.0025$ K).

[1] JCMT is operated by the JAC, Hawaii, on behalf of the UK PPARC, the Netherlands OSR, and the Canadian NRC, see http://www.jach.hawaii.edu/JCMT/.
[2] http://www.dlh.pmo.cas.cn/
[3] http://www.submm.caltech.edu/cso/
[4] http://iram.fr/IRAMFR/GILDAS/
[5] Available at http://irsa.ipac.caltech.edu/; see also Benjamin et al. (2003).
[6] http://irsa.ipac.caltech.edu/
[7] http://www4.cadc-ccda.hia-iha.nrc-cnrc.gc.ca
[8] The SMA is a joint project between the Smithsonian Astrophysical Observatory and the Academia Sinica Institute of Astronomy and Astrophysics and is funded by the Smithsonian Institution and the Academia Sinica; see http://www.cfa.harvard.edu/sma/.

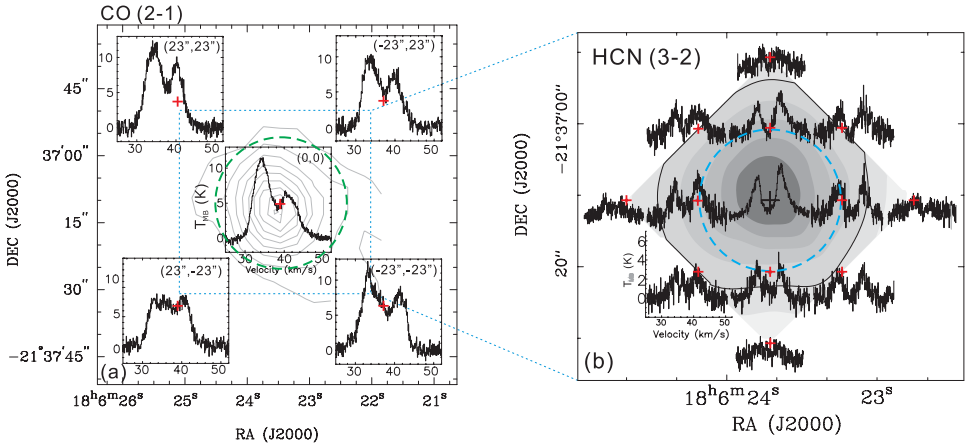

Figure 2. (a) Grid spectra of ^{12}CO (2 − 1) observed from the CSO. The red cross labels the pointing centre of each spectrum. The grey contours are the SCUBA 450 μm emission (specified in Fig. 4). The green dashed line represents the beam size. (b) Grid spectra of HCN (3 − 2) observed from the JCMT. The red cross labels the pointing centre of the each spectrum. The intensity map (grey-scales) is made from interpolating the line intensity at each point. The integration for the spectra is from 25 to 50 km s^{-1}. The grey-scale levels are from 30 per cent to 90 per cent of the maximum intensity (46.8 K km s^{-1}). The thick contour is the 50 per cent level. The blue dashed circle is the beam size.

Table 1. General information of the single-dish observations.

Instrument	PMO	CSO	JCMT
Observation date	Dec. 2009	2011 May	2005 Aug
Beam size	56 arcsec	30 arcsec	21 arcsec
η_{mb}	0.62	0.698	0.63
Pointing centre	RA = 18^h 06^{s}22^s.87	RA = 18^h 06^{m}23^s.5	RA = 18^h 06^{m}23^s.46
	Dec.=−21° 37′20″.7	Dec.=−21° 37′10″.7	Dec.=−21° 37′09″.64

Table 2. Observational parameters for the molecular lines from the single dishes.

Transition	Instrument	Atmosphere opacity	Bandwidth (MHz)	ΔV_{res} (km s^{-1})	rms noise per channel (K)
^{12}CO (2 − 1)	CSO	0.167	500	0.079	0.2
^{13}CO (2 − 1)	CSO	0.152	500	0.083	0.2
C^{18}O (2 − 1)	CSO	0.149	500	0.083	0.2
^{12}CO (1 − 0)	PMO	0.015	145	0.370	0.1
^{13}CO (1 − 0)	PMO	0.015	43	0.115	0.1
C^{18}O (1 − 0)	PMO	0.015	43	0.115	0.2
HCN (3 − 2)	JCMT	0.111	160	0.088	0.5
H^{13}CO$^+$ (3 − 2)	JCMT	0.067	160	0.090	0.3

Table 3. Observational parameters of the SMA.

Epoch	Frequency bands (GHz) LSB, USB	Bandpass calibrator	Flux calibrator	Phase and synthesized calibrator	Beam size (arcsec)	rms noise per channel (K)[a]
2007	(279.4, 281.4), (289.4, 291.4)	3c273	Neptune	1733-130, 1911-201	7.0 × 5.8	0.110
2008	(219.5, 221.5), (229.5, 231.5)	3c454.3	Neptune	1733, 1911	4.8 × 3.6	0.017
2009	(217.5, 219.5), (227.5, 229.5)	3c273	Uranus	1733, 1911	6.8 × 3.6	0.150

[a]For the unit conversion, 1 K = 0.367, 1.43 and 1.04 Jy beam^{-1} for the data in 2007, 2008 and 2009, respectively.

3 RESULTS

3.1 Dust continuum emission

In Fig. 4, we show the continuum emissions of G8.68 from infrared to (sub)millimetre wavebands, including the IRAC 3.6, 4.5 and 8 μm emissions [Red-Green-Blue (RGB) colour image], the SMA 1.3 mm continuum emission (white contours) and the SCUBA 450 μm continuum (blue dashed contours).

Fig. 4 is centred at the 1.3 mm continuum peak, the coordinates of which are RA (J2000) =18^{h}06^{m}23.52^s, Dec. (2000) =−21°37′11″. It is close in projection to the SMA phase tracking centre (labelled with the red cross). After deconvolution with the synthesized beam, the core has an angular size of 11 × 6 arcsec^2 for the 4σ contour

(0.24 × 0.13 pc at a distance of 4.5 kpc). It is elongated in the north–south direction (position angle, PA = −10° for the major axis), reasonably coherent with the 4.5 μm emission (green colour). Since the 4.5 μm emission traces the shock interaction between the outflow and the envelope gas, it is possible that the outflow and shocks are also affecting the dust distribution, causing its observed elongation. We did not find any evidence for multiple subcores either in our 1.3 mm continuum or in any molecular lines (as shown in Fig. 5). Therefore the gas-and-dust core should have a single compact morphology, and the fragmentation is not evident on our observational scale (0.05–0.5 pc).

More diffused dust components can be revealed by the SCUBA 450 μm continuum emission. As shown in Fig. 4, the 450 μm emission is more extended and less elongated than the 1.3 mm emission. We use the average deconvolved full width at half-maximum (FWHM) radius $\langle r \rangle$ to represent the extent of the continuum and molecular line emissions. Normally, $\langle r \rangle$ can be measured from the 50 per cent contour level of the emission region. However, the 50 per cent contour (for the continuum and molecular lines) is often close to, or even smaller than, beam size. We thus suggest measuring the deconvolved radius from the 10 per cent contour and adopt its 1/2 as the value of $\langle r \rangle$. For the continuum images, the 10 per cent contour is not specifically plotted in Fig. 4, but is close to the 14σ and 4σ contour levels for the 1.3 mm and 450 μm emissions, respectively. We obtained $\langle r \rangle_{450\,\mu\mathrm{m}} = 0.23$ pc and $\langle r \rangle_{1.3\,\mathrm{mm}} = 0.08$ pc.

We also measured the integrated flux density $F(\lambda)$ of the dust core at wavelength λ. In general, we use the 4σ emission level as the integration area for $F(\lambda)$. As an exception, for the IRAC data, we use the region of the 4.5 μm emission (green colour in Fig. 4) to measure the integrated flux of all four bands, since the 4.5 μm emission has a relatively clear boundary. The 5.8 μm band shows a similar morphology to the 4.5 μm, while the emissions at the other two bands are much fainter and cannot be well delineated. The IRAC stellar sources in the vicinity of the core are carefully excluded from the integration area. The derived $F(\lambda)$ are shown in Table 4.

Table 4. Physical parameters of the dust core.

Parameter	Value	Unit
F (3.6 μm)	13 ± 0.1	mJy
F (4.5 μm)	78 ± 2	–
F (5.8 μm)	68 ± 2	–
F (8.0 μm)	10 ± 1	–
F (24 μm)	657 ± 40	–
F (70 μm)	196 ± 15	Jy
F (450 μm)	144 ± 15	–
F (850 μm)	15 ± 4	–
F (1.3 mm)[a]	0.65 ± 0.03	–
F (1.3 mm)[b]	2.9	–
	(450 μm/1.3 mm)[c]	
$\langle r \rangle$	0.23 ± 0.05/0.08 ± 0.02	pc
M_{core}	1.5 ± 0.2/0.30 ± 0.01	10^3 $M_\odot$
$N(H_2)$	1.2 ± 0.2/0.95 ± 0.03	10^{24} cm^{-2}
$n(H_2)$	0.8 ± 0.1/3.8 ± 0.3	10^6 cm^{-3}

Note. To measure the integrated flux density of the dust core, we use the 4σ emission level as the integration area (aperture for the photometry). As an exception, we use the 4σ level of the 4.5 μm emission as the area for all four IRAC bands, which roughly equals the emission region with green colour in Fig. 4. The nearby point sources have been carefully excluded from this aperture.

[a]The flux density of the SMA continuum observation.

[b]The flux density extrapolated from the SED fitting (Fig. 6).

[c]For the last four parameters, the first and second values are derived from the 450 μm and 1.3 mm continuum data, respectively.

3.2 Molecular lines

3.2.1 The Submillimeter Array

Using the SMA, we have detected a number of molecular transitions of $C^{18}O$, $C^{34}S$, DCN and CH_3OH. Their beam-averaged spectra towards the 1.3 mm continuum peak and their velocity-integrated intensity images are shown in Fig. 5. For CH_3OH, altogether we have detected 11 rotational transitions. We have selected five with largely different E_u and presented their images in Fig. 5. The physical parameters of all the molecular transitions are shown in Table 5.

As shown in Fig. 5, the spectra of the molecular tracers of high-density gas mostly show lines with single-peak profiles. As exceptions, there are two CH_3OH lines, $11_2 - 10_3$ ($E_u = 191$ K) and $15_{7,8} - 16_{6,11}$ ($E_u = 523$ K), which show double-peak profiles. However, since the remaining lines are all single peaked, the two lines are more likely to be blended with other molecular transitions. The possible candidates for the blenders are NH_2CN $14_2 - 13_2$ ($f = 279.350\,62$ GHz, $E_u = 228$ K) and HCCNC $29 - 28$ ($f = 288.073\,46$ GHz, $E_u = 207$ K). We used two Gaussian profiles to fit the blended spectra as plotted in dotted lines in Fig. 5. For each spectrum, the peak velocity of the second component is consistent with the anticipated velocity for the blenders. With the contamination excluded, these two CH_3OH lines should also have single-Gaussian profiles.

The $C^{34}S$ emission region shows an elongated morphology from the north-east to south-west (PA = 45°) as labelled in the dashed line. The elongation agrees with the orientation of the CO outflow and 4.5 μm shock emission (Fig. 4). An elongated morphology towards north-east is also shown in the low-excited CH_3OH lines (i.e. $E_u = 33$ K and 97 K). Therefore, both the CH_3OH and $C^{34}S$ distributions should be affected by the outflow. The $C^{18}O$ $(2-1)$ also shows a non-regular morphology. However, it is biased to the south of the dust core, peaked at offset= (0, −2arcsesc). In addition, the $C^{18}O$ shows a secondary clump in the south-east, peaked at offset= (10, −8arcsesc). This clump is not detected in $C^{34}S$ or CH_3OH lines, indicating that it may be depleted in these species. The $C^{18}O$ might trace a cooler and less dense gas component, thus have a more extended feature than other dense-core species. For each molecular transition, we also measured the average deconvolved radius from the 10 per cent contour level (and adopted its 1/2 as the value of $\langle r \rangle$). The results are shown in Table 5.

3.2.2 The single dishes

Figs 2 and 3 show the molecular lines detected from the single dishes. As shown in Fig. 3, prominent double-peak line profiles are observed in the ^{12}CO $(1-0)$, $(2-1)$ and also in HCN $(3-2)$. For both the ^{12}CO $(1-0)$ and $(2-1)$, the blueshifted emission peak is much stronger than the redshifted one, and the central absorption dip is well coincident with the $C^{18}O$ line peak ($V_{\mathrm{lsr}} = 37$ km s^{-1}). Such blue asymmetric ^{12}CO lines suggest the presence of infall motion towards the core centre (Zhou et al. 1993; Mardones et al. 1997). For the physical explanation, when the infall occurs in the envelope

Table 5. Observed parameters of the molecular lines.

Molecule	Transition	Rest frequency (GHz)	E_u (K)	V_{LSR} (km s^{-1})	$T_{b,peak}$ (K)	ΔV_{FWHM} (km s^{-1})	$\int T_b dV$ (K km s^{-1})	τ^a	$\langle r \rangle^b$ (arcsec)	η_{bf}^c
(1)	(2)	(3)	(4)	(5)	(6)	(7)	(9)	(8)	(10)	(11)
^{12}CO(core)	1 − 0	115.271 20	5.5	37.0	26.0(1.5)	5.0(0.5)	134(15)	75	–	–
^{12}CO(outflow)	1 − 0	–	–	37.3	4.0(1.5)	9.2(1.0)	37(5)	0.15	–	–
^{12}CO(core)	2 − 1	230.538 00	17	37.0	32.0(0.5)	5.5(0.5)	240(30)	68	–	–
^{12}CO(outflow)	2 − 1	–	–	37.0	5.0(0.5)	9.0(0.5)	45(6)	0.15	–	–
HCN(core)	3 − 2	265.886 43	26	38.5	12.0(0.2)	6.2(0.5)	73(9)	0.78/0.10	12	1
HCN(outflow)	3 − 2	–	–	39.5	0.8(0.2)	15.0(1.0)	12(5)	0.053/0.007	–	–
^{13}CO	1 − 0	110.201 35	5.3	35.0	12.4(0.5)	6.8(0.1)	85(10)	0.85	–	–
^{13}CO	2 − 1	220.399 68	16	35.0	8.5(0.5)	7.5(0.5)	60(15)	0.70	–	–
C^{18}O	1 − 0	109.782 17	5.3	37.0	4.5(0.5)	5.6(0.4)	23(4)	0.17	–	–
C^{18}O(CSO)	2 − 1	219.560 36	16	38.0	6.0(0.3)	5.5(0.4)	34(3)	0.140	–	–
C^{18}O(SMA)	2 − 1	219.560 36	16	38.0	5.2(0.02)	4.8(0.3)	30(3)	0.423/0.065	3.4	1
CH_3OH	$8_0 - 7_1$	220.078 49	97	37.5	1.6(0.22)	5.0(1.3)	8(2)	0.209/0.028	3.1	1
CH_3OH	$8_{-1} - 7_0$	229.758 80	89	37.0	3.42(0.15)	6.0(0.3)	18.0(1.5)	0.453/0.059	2.8	1
CH_3OH	$3_{-2} - 4_{-1}$	230.027 06	39	38.5	0.9(0.03)	6.0(0.4)	5.8(0.5)	0.036/0.004	3.2	1
CH_3OH	$10_2 - 9_3$	231.281 10	165	39.0	0.53(0.06)	6.0(0.9)	3.4(0.5)	0.087/0.011	2.2	0.95
CH_3OH	$9_{-1} - 8_0$	278.304 51	110	38.0	1.39(0.06)	5.4(0.4)	7.2(0.8)	0.245/0.031	2.9	0.89
CH_3OH	$2_{-2} - 3_{-1}$	278.342 26	33	39.0	0.24(0.02)	5.5(0.4)	1.5(0.2)	0.045/0.006	3.2	1
CH_3OH	$21_{-2} - 20_{-3}$	278.480 23	563	40.0	0.09(0.02)	4.0(0.5)	0.4(0.05)	0.024/0.002	2.2	0.48
CH_3OH	$15_{7,8} - 16_{6,11}$	288.076 77	523	37.5	0.24(0.02)	5.5(0.3)	1.2(0.2)	0.102/0.012	2.3	0.52
CH_3OH	$14_4 - 15_3$	278.599 06	340	39.5	0.29(0.02)	6.3(1.3)	1.8(0.2)	0.073/0.009	2.5	0.62
CH_3OH	$11_2 - 10_3$	279.351 91	191	39.5	0.28(0.02)	6.5(1.9)	2.3(0.3)	0.081/0.009	2.8	0.78
CH_3OH	$4_3 - 5_2$	288.705 57	71	39.5	0.28(0.02)	6.5(1.5)	1.8(0.3)	0.068/0.008	2.8	0.77
DCN	3 − 2	217.238 54	81	39.0	2.1(0.4)	3.5(0.2)	7.5(1)	0.132/0.018	3.1	0.92
DCN	4 − 3	289.644 92	35	39.0	1.0(0.04)	3.5(0.2)	5.0(0.4)	0.072/0.009	3.3	1
C^{34}S	6 − 5	289.209 07	38	39.0	1.4(0.02)	4.5(0.5)	6.5(0.7)	0.123/0.016	3.3	1
H^{13}CO$^+$	3 − 2	260.255 34	25	38.0	4.7(0.3)	4.4(0.3)	20(2)	0.260/0.033	–	–

Note. The ^{12}CO, ^{13}CO lines and C^{18}O lines are from the PMO and CSO observations (see Table 2). The C^{18}O (2 − 1) line from the SMA observation is also presented. The HCN and H^{13}CO$^+$ lines are observed with the JCMT. For the double-peaked lines, including HCN (3 − 2), ^{12}CO (2 − 1) and (1 − 0), and two CH_3OH lines (E_u = 191 K and E_u = 523 K), the parameters are measured from the fitted spectra, while for the single-peak lines, we directly measured the observed spectra.

[a]The optical depth at the line peak. For the transitions with two values, the first and second one are the results for T_{rot} = 20 and 114 K, respectively (see Section 4.4). While for the CO (1 − 0) and (2 − 1), the optical depths are calculated from comparing their isotopic lines (Section 4.3).

[b]The effective radius of the emission region, measured from the deconvolved average radius of the 10 per cent contour region (1/2 times the value). An exception is the HCN (3 − 2), for which we directly measured the 50 per cent contour. The average uncertainty level is ∼2 arcsec. For G8.68 at D =4.5 kpc, 1 arcsec=0.02 pc.

[c]The beam-filling factor, calculated from the ratio between the area of the deconvolved emission region ($\pi \langle r \rangle^2$) and the beam size.

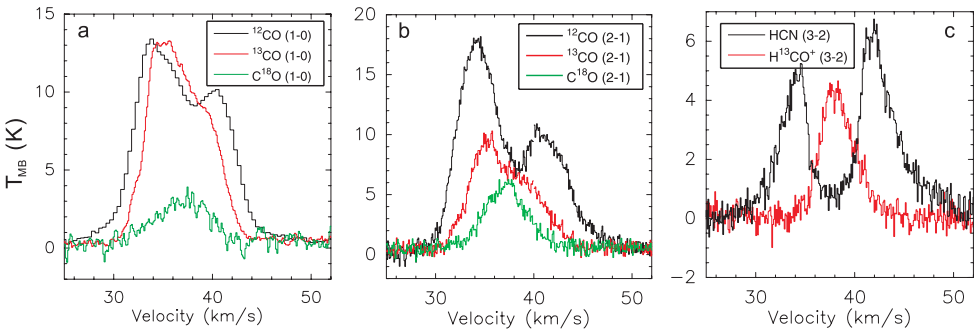

Figure 3. Molecular lines observed from the PMO, CSO and JCMT, which are shown in the left-hand, middle and right-hand panels, respectively. The observing centers and the beam size of each telescope are shown in Fig. 1.

which is cooler than the inner region, the gas in the front part would absorb the redshifted side of the line profile, whereas the gas in the rear part (behind the centre) would increase the blueshifted emission because it is moving towards the observer. Besides the infall signature, the ^{12}CO lines also exhibit high-velocity emission wings extending to V_{lsr} =25 and 50 km s^{-1} for the blueshifted and redshifted sides, respectively. This velocity range is comparable to the outflow velocities revealed by L11 (fig. 5 therein).

The two ^{13}CO lines also have a blueshifted emission peak (V_{lsr} = 35 km s^{-1}) with respect to the C^{18}O, suggesting that the ^{13}CO is also probably tracing the infall motion. However, because the ^{13}CO lines are much less optically thick than the ^{12}CO, they exhibit no

central dip, but instead show an emission shoulder that continuously declines towards the redshifted side.

As shown in Fig. 2(a), we can see that the offset positions also exhibit self-absorbed profiles (except the south-east one). However, compared to the central spectrum, their blueshifted and redshifted peaks have more similar intensities. As an extreme, the south-eastern spectrum has a flattened top, with the double-peak feature almost disappeared. This indicates that the infall motion (along the line of sight) should have a decline towards those offset points. And their distance from the centre (0.7 pc) can therefore be taken as a lower limit for the radius of the infalling region.

As shown in Fig. 3(c), the HCN (3 − 2) has a double-peak profile and high-velocity emission wings extending to $V_{\rm lsr} = 29$ and 53 km s^{-1} (above the noise level) for the blue and red wings, respectively. However, its double peaks have different asymmetry with the ^{12}CO lines, i.e. the red peak is slightly stronger than the blue one. The offset spectra of the HCN (Fig. 2b) have a much lower signal-to-noise ratio (mainly due to their shorter integration time). However, they still evidently show double-peak profiles and have similar intensities for the blue and red peaks. As in the case of the CO lines, the optically thin isotopic lines, i.e. DCN (3 − 2) and (4 − 3) are both single peaked; hence the HCN (3 − 2) profile should originate from a self-absorption effect. Compared to the ^{12}CO profiles, the HCN spectra may reflect different gas motions, including core expansion or/and rotation (Pavlyuchenkov et al. 2008). In particular, as the most possible case, a cold and spherically expanding envelope would cause a prominent blueshifted self-absorption towards the centre, while at the offset positions, the expansion should be on the plane of the sky, thus show a less blueshift due to the lower radial velocities. This scenario can reasonably explain the observed line profiles, but it still needs a further examination with an improved angular resolution and spectral sensitivity. In Fig. 2(b), we also plot the velocity-integrated map of HCN (3 − 2) (discrete grey-scales). We measured the average deconvolved radius $\langle r \rangle$ of HCN from its 50 per cent contour. As a result, it has $\langle r \rangle = 12$ arcsec (and $\eta_{\rm bf} = 1$).

Another JCMT line, H^{13}CO$^+$ (3 − 2), has a regular Gaussian profile, indicating that it may arise from the dense molecular core and is not evidently affected by the infall or outflow motion. We only have one-point observation for the H^{13}CO$^+$ (3 − 2) at the continuum centre, and in the calculation its column density (Section 4.4), we assume $\eta_{\rm bf} = 1$.

4 DISCUSSION

4.1 The physical properties of the dust core

As shown in Fig. 4, the 1.3 mm dust core does not coincide with any infrared stellar sources besides the extended 4.5 μm shock emission. This indicates that the stellar emission from the core centre is highly obscured by the dust. In the vicinity of the 1.3 mm dust core, a few stellar objects are shown in the IRAC RGB image (also labelled with the asterisks). All these objects are isolated from the 1.3 mm continuum emission; yet the three objects nearest to the continuum peak are likely to be embedded in the 450 μm emission region. They might either be more evolved young stars in the same star-forming region or irrelevant foreground stars. Despite this uncertainty, it is clear that these objects have no significant contribution to the dust continuum or molecular line emissions. We therefore make no further discussion for them.

We can fit the spectral energy distribution (SED) of the dust core from its flux densities at the *Spitzer* and JCMT/SCUBA wavebands.

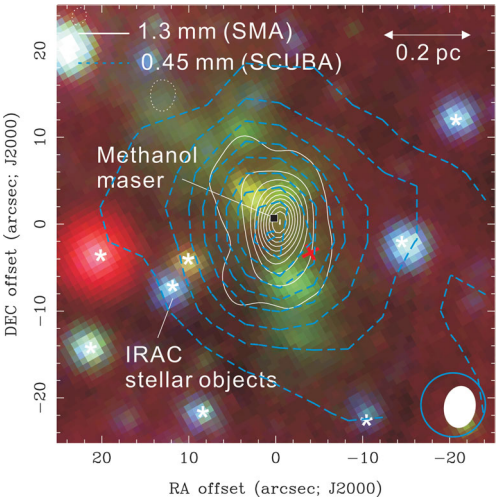

Figure 4. Continuum emissions detected towards G8.68 from infrared to millimetre wavelengths. The image is centred at the emission peak of the 1.3 mm continuum, the coordinates of which are RA (J2000) = $18^{\rm h}06^{\rm m}23.5^{\rm s}$ and Dec. (J2000) = −21°37′10.7″. The white contours are the 1.3 mm emission observed from the SMA. The contour levels are −4, 4, 14, 24,..., 104σ (0.003 Jy beam^{-1}). The −4σ contour is due to the insufficient (u, v) coverage and is plotted with the dotted line. The square denotes the strongest CH_3OH maser (Walsh et al. 1998). The dashed contours are the JCMT/SCUBA 450 μm emission. The levels are 4, 8, 12,..., 36σ (1.2 Jy beam^{-1}). The IRAC 3.6 (blue), 4.5 (green) and 8.0 (red) μm images are shown together in RGB colours (also seen in figs 1 and 2 in L11). The red cross labels the SMA phase centre. The synthesized beam of the SMA (white ellipse) and SCUBA (blue circle) beam are plotted on the right-hand corner.

Assuming a grey-body emission and a uniform dust temperature $T_{\rm d}$, the continuum flux density would be (Schnee et al. 2007)

$$F_\nu = \frac{M_{\rm core}\kappa_\nu B_\nu(T_{\rm d})}{g D^2}, \quad (1)$$

where F_ν is the flux density at frequency ν. $M_{\rm core}$ is the total gas-and-dust mass of the core, $g = 100$ is commonly adopted gas-and-dust mass ratio, $B_\nu(T_{\rm d})$ is the Planck function at temperature $T_{\rm d}$ and $D = 4.5$ kpc is the source distance. The dust opacity κ_ν is assumed to have a power-law shape, i.e. $\kappa_\nu = \kappa_{230\,\rm GHz}(\nu/230\,\rm GHz)^\beta$, with the reference value $\kappa_{230\,\rm GHz} = 0.9\,\rm cm^2\,g^{-1}$ (Ossenkopf & Henning 1994). The free parameters in the fit are $M_{\rm core}$, $T_{\rm d}$ and β. We found that the emissions from 8 to 850 μm can be best fitted with two temperature components which have $T_{\rm d} = 20$ and 120 K, respectively, and $\beta = 2.1$. The best-fitting SED is shown in Fig. 6.

We did not include the IRAC 3.6, 4.5 or 5.8 μm emissions in our SED model. The 4.5 and 5.8 μm emissions may largely come from the shocked emission, and thus are much stronger than the emissions at other two IRAC bands (Table 4). As for the 3.6 μm emission, if being thermally excited, it may arise from some even hotter component which is much fainter and poorly constrained by our current data. Therefore we also neglected the 3.6 μm band. With the derived SED, the bolometric luminosity can be estimated using $L_{\rm bol} = 4\pi D^2 \int F_\nu {\rm d}\nu$. As a result, we have $L_{\rm bol} = 2.3 \times 10^4$ and $8 \times 10^2\,L_\odot$ for the cold (20 K) and warm (120 K) components, respectively. Using equation (1), we can also estimate the total mass of the two temperature components, which turn out to be 1.3×10^3 and $1.0 \times 10^{-3} M_\odot$ for the 20 and 120 K components, respectively. One can see that both the core mass and luminosity are dominated by the gas-and-dust component which is characterized by $T_{\rm d} = 20$ K.

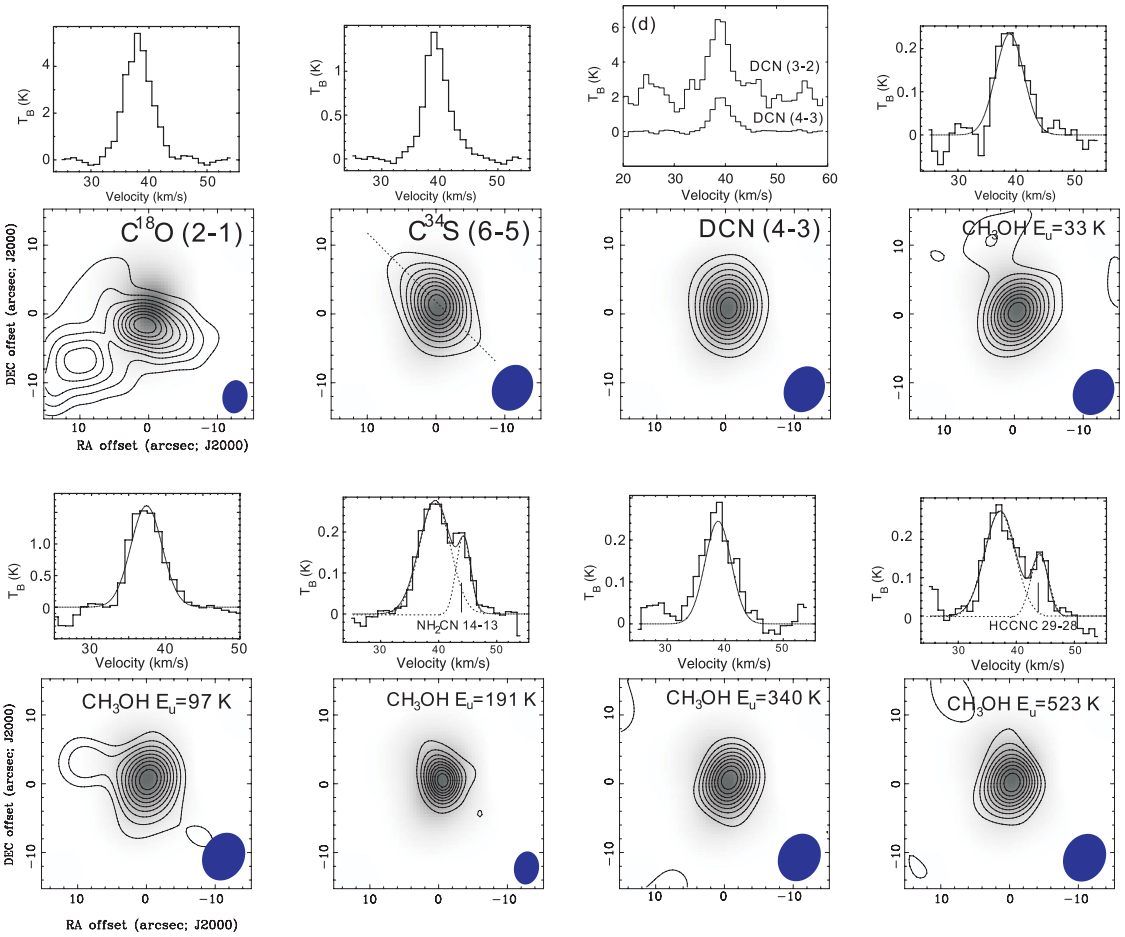

Figure 5. Molecular lines and integrated images observed from the SMA. For each transition, the contours are 10, 20,..., 90 per cent of the peak intensity. The integration range is (37, 43) km s^{-1} for all the transitions except the two blended CH_3OH lines. For these two lines the integration range is (37, 40) km s^{-1} as to eliminate the contamination. The dashed line in the $C^{34}S$ labels the orientation of the outflow in L11. The DCN (3 − 2) line is shifted above the zero level for 2 K. The negative contours due to the missing flux are omitted to more clearly show the emission features. The grey-scale image in each panel is the SMA 1.3 mm continuum.

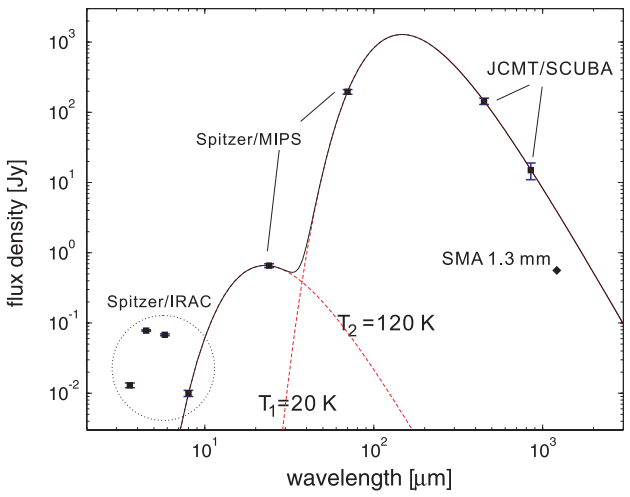

Figure 6. The spectra energy distribution of the dust core. The black squares with error bars are the data points (the SMA 1.3 mm flux density is marked with the diamond). The black line is the fitted SED curve. The red dashed lines are the SEDs of the two temperature components, with $T_d = 20$ and 120 K, respectively.

In equation (1), by replacing the integrated flux density F_ν with the flux density at the continuum peak (0.32 Jy beam^{-1}), and then dividing the obtained mass by the beam area and the average molecular mass (1.4 times the molecular mass of H_2), we can derive the H_2 column density $N(H_2)$ towards the continuum peak. And then, assuming that the core is approximately spherical, we can derive the volume number density using $n(H_2) = N(H_2)/2\langle r\rangle$. The physical parameters of the dust core are presented in Table 4.

By extrapolating the best-fitting SED curve, we get a flux density of 2.9 Jy at $\lambda = 1.3$ mm. Compared to this value, the SMA observation has recovered 35 per cent of the 1.3 mm continuum emission. Adopting $T_d = 20$ K, we also estimated the physical parameters from the SMA 1.3 mm continuum, which are presented in Table 4. Based on the continuum observations, we suggest that the gas-and-dust core in G8.68 should consist of a dense inner region (characterized by the 1.3 mm emission) and a more extended envelope (traced by the 450 μm emission).

4.2 The CH_3OH rotational temperature

The molecular gas temperature can also be estimated from the CH_3OH lines using the rotation diagram. The methanol lines all

have linewidths of several km s^{-1}, with none of them showing abnormally high intensities; therefore, the CH_3OH lines are unlikely to have maser excitations.

Assuming optically thin, the column density of the upper level N_u can be derived from the integrated line intensity using (Tielens 2005)

$$N_u = \frac{8\pi k \nu_{ul}^2}{hc^3 A_{ul}} \int T_b dV / \eta_{bf}, \quad (2)$$

where T_b is the observed brightness temperature. A_{ul} is the Einstein coefficient in s^{-1}. η_{bf} is the beam-filling factor. All other constants take their usual values in SI units. Although for an emission line, η_{bf} may vary at different velocities, we approximate it to be a single value, as the ratio between the integrated emission region and the beam area, i.e. $\eta_{bf} \simeq \pi\langle r\rangle^2/A_{beam}$ (used when the emission region is smaller than the beam size; otherwise $\eta_{bf} = 1$). η_{bf} is estimated for each transition and the derived values are presented in Table 5 (column 11).

Assuming a local thermal equilibrium (LTE, i.e. energy levels are populated according to a Boltzmann distribution characterized by a single temperature), the relation between the total column density N_T and N_u is

$$\frac{N_u}{g_u} = \frac{N_T}{Q(T_{rot})} \exp\left(-\frac{E_u}{kT_{rot}}\right), \quad (3)$$

and its logarithmic form is

$$\ln\left(\frac{N_u}{g_u}\right) = \ln\left(\frac{N_T}{Q(T_{rot})}\right) - \frac{E_u}{kT_{rot}}, \quad (4)$$

where g_u and E_u are the degeneracy and the excitation energy of the upper level, respectively, and $Q(T_{rot})$ is the partition function. For CH_3OH, a good approximation is $Q(T_{rot}) \simeq 1.2327 \times T_{rot}^{1.5}$ (Townes & Schawlow 1955).

The rotation diagram for the CH_3OH lines is shown in Fig. 7. A linear least-squares fit to the data points results in $T_{rot} = 130 \pm 10$ K and $N_T = (5.3 \pm 0.6) \times 10^{15}$ cm^{-2}.

In the calculation, in order to correct for the optical depth effect, one should multiply N_u/g_u with a correction factor $C_\tau = \tau/(1 - e^{-\tau})$ and fit the rotational temperature iteratively. The optical depth is estimated using (Remijan et al. 2004, equation 3 therein, slightly reformed)

$$\tau = \frac{c^3\sqrt{4\ln 2}}{8\pi\nu^3\sqrt{\pi}\Delta V} N_u A_{ul} \left[\exp\left(\frac{h\nu}{kT_{rot}}\right) - 1\right]. \quad (5)$$

Among all the CH_3OH lines, the $(8_{-1} - 7_0)$ transition has the highest optical depth ($\tau = 0.059$). The other lines are even more optically thin. To take into account the temperature uncertainty, we also estimated the optical depth assuming $T_{rot} = 20$ K which is a lower limit as suggested by the SED fitting. At 20 K, the optical depths become ~8 times larger than the values at $T_{rot} = 130$ K. The derived optical depths are listed in Table 5, and the column densities and abundances are listed in Table 6.

The rotational temperature of $T_{rot} = 130$ K is close to the SED temperature of the warm dust component ($T_d = 120$ K). Therefore it is possible that the CH_3OH emissions are mainly from the region associated with the warm dust. Moreover, since the cold component ($T_d = 20$ K) is more massive than the warm one for orders of magnitude, the CH_3OH may have a severe depletion in the region for the cold dust component. However, it is also possible that the dust and gas are thermally decoupled, thus exhibit different temperatures. The collisional excitations of the molecular gas can be particularly enhanced by the shocks (especially along the outflow direction), thereby showing a high value of T_{rot}. The dust temperature T_d, in comparison, may still be largely dominated by the stellar heating thus has a much lower value.

4.3 The CO emission and the infall motion

As shown in Section 3.2.2, both the infall and outflow signatures are detected in the ^{12}CO (2 − 1) and (1 − 0) lines. In this paper we mainly discuss the infall properties based on the ^{12}CO (2 − 1). We first make attempt to separate the different components from the observed spectrum, then estimate the infall rate.

Following the procedure of Purcell et al. (2006), we used a broad Gaussian profile to fit the outflow wings (velocity range of $V < 32$ and $V > 42$ km s^{-1}) and then subtracted it from the spectrum. The residual line profile (green line in Fig. 8) should mainly represent the emission from the dense molecular core. One can then mask the velocity range possibly affected by the infall motion (34–43 km s^{-1}) and make a Gaussian fit to the spectrum outside this velocity range. The fitted spectrum is speculated to roughly represent the molecular core emission unaffected by the infall signature. However, for the ^{12}CO lines, due to its large optical depth, we cannot directly apply a Gaussian fit to the spectrum. Instead, one should model the spectrum

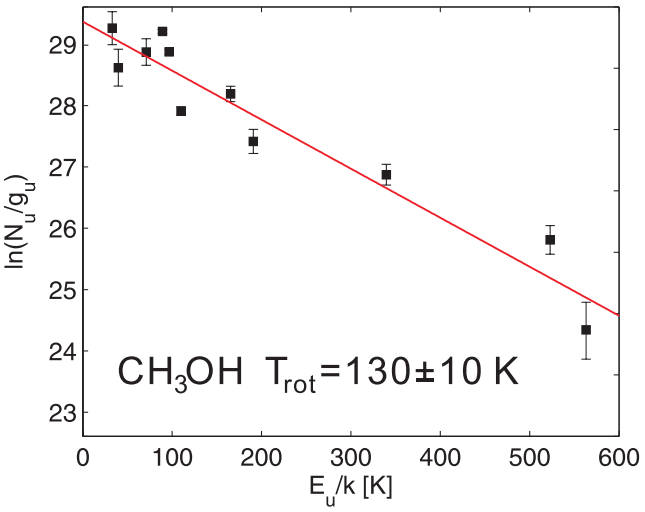

Figure 7. The rotation diagram of the CH_3OH lines. The black squares with error bars are the data points. The red line is the least-squares fit.

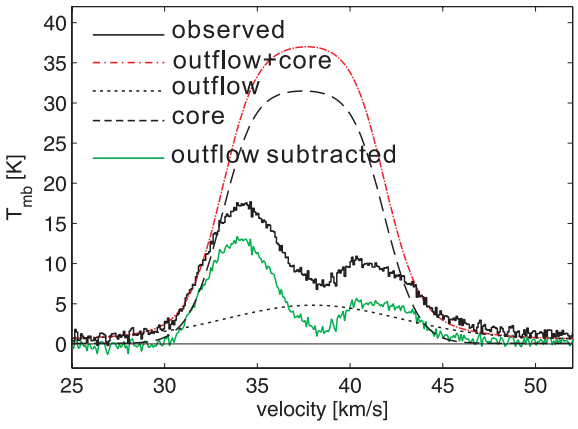

Figure 8. The two-component fit to the ^{12}CO (2 − 1) spectrum towards the centre. The meaning of each line type is labelled in the legend.

using the radiation transfer function. In this case, the line profile can be expressed as

$$T_{\rm mb}(V) = [T_{\rm mb,0} - J(T_{\rm CMB})][1 - {\rm e}^{-\tau(V)}]. \quad (6)$$

$J(T) = T_0/[\exp(T_0/T) - 1]$ is the *Planck*-corrected brightness temperature and $T_0 = h\nu/k$. $T_{\rm CMB} = 2.7$ K is the temperature of the cosmic background. At the frequency of CO (2 − 1) (230 GHz), we have $J(T_{\rm CMB}) = 0.2$ K. Compared to the intensity of the CO emission, the contribution from the cosmic background can be almost neglected.

We also assume the dense molecular core to have a uniform gas distribution along the line of sight, with the central velocity V_0, velocity dispersion σ and peak optical depth τ_0. Then the optical depth is

$$\tau(V) = \tau_0 \exp\left[-\frac{(V - V_0)^2}{2\sigma^2}\right], \quad (7)$$

where σ is related to the (intrinsic) linewidth ΔV by $\sigma = \Delta V/\sqrt{8\ln 2}$. In an optically thick case, the line emission could be largely saturated. τ_0 is thus poorly constrained by the observed spectrum. However, it can be estimated from comparison to the CO isotopologues following Garden et al. (1991, equation 4 therein). Since the ^{13}CO is also affected by the infall motion, we used the C^{18}O (2 − 1) instead. Assuming an abundance ratio of [^{12}CO/C^{18}O] = 490 (Garden et al. 1991), the equation will be

$$\frac{T_{\rm mb,0}(^{12}{\rm CO})}{T_{\rm mb,0}({\rm C}^{18}{\rm O})} = \frac{1 - \exp[-\tau_0(^{12}{\rm CO})]}{1 - \exp[-\tau_0({\rm C}^{18}{\rm O})]} = \frac{1 - \exp[-\tau_0(^{12}{\rm CO})]}{1 - \exp[-\tau_0(^{12}{\rm CO})/490]}. \quad (8)$$

To fit the line profile, we first take an arbitrary, but reasonable value of τ_0 and then fit the line profile by adjusting the values of $T_{\rm mb,0}$, V_0 and ΔV in equations (6) and (7). The best-fitting $T_{\rm mb,0}$ is then used to estimate τ_0 again using equation (8). The final best fit can be reached after two or three iterations. Eventually, we have $T_{\rm mb,0} = 32$ K, $\Delta V = 5.5\,{\rm km\,s^{-1}}$, $V_0 = 37\,{\rm km\,s^{-1}}$ and $\tau_0(^{12}{\rm CO}) = 68$. In Fig. 8, the best-fitting spectrum is shown by the dashed line. And a sum of dense-core and outflow components is shown by the red dot–dashed line. The output spectrum has an apparent linewidth of $8.5\,{\rm km\,s^{-1}}$ which is indeed much broader than the intrinsic ΔV. We fit the ^{12}CO (1 − 0) using the same method. All their line parameters are listed in Table 5 (columns 5–8).

The infall rate is estimated using (Klaassen & Wilson 2007)

$$\dot{M}_{\rm inf} = \frac{4}{3}\pi n({\rm H_2})\mu m_{\rm H} r_{\rm gm}^2 V_{\rm in}, \quad (9)$$

where $r_{\rm gm}$ is the geometric mean radius of the core, $n(H_2)$ is the ambient source density and $V_{\rm in}$ is the typical infall velocity. In calculation, we estimated $V_{\rm in}$ from the outflow-subtracted line profile using equation (9) in Myers et al. (1996). As a result, we have $V_{\rm in} = 0.45\,{\rm km\,s^{-1}}$. In addition, we assume that the more diffused gas traced by the 450 μm emission which has $n(H_2) = 0.8 \times 10^6\,{\rm cm^{-3}}$, is collapsing towards the dense inner region characterized by the 1.3 mm continuum (Fig. 4); thus we have $r_{\rm gm} = \langle r\rangle_{1.3{\rm mm}} = 0.08$ pc. With these assumptions, we derived an infall rate of $\dot{M}_{\rm inf} = 7.0 \times 10^{-4} M_\odot\,{\rm yr^{-1}}$.

As seen in equation (9), the derived infall rate is sensitive to the adoption of $r_{\rm gm}$, and our currently adopted $r_{\rm gm}$ is relatively conservative. Adopting $r_{\rm gm} = \langle r\rangle_{450\mu{\rm m}} = 0.23$ pc, we would have $\dot{M}_{\rm inf} = 5 \times 10^{-3} M_\odot\,{\rm yr^{-1}}$. However, we note that such a large-scale estimate may deviate from the small-scale infall rate. To resemble the mass infall on to the central stars, it may be more reasonable to adopt the first value ($r_{\rm gm} = 0.08$ pc). With the obtained infall rate, we then estimate the accretion luminosity, using $L_{\rm acc} = GM_\star\dot{M}_{\rm inf}/R_\star$, and assuming a mass–radius relation of $R_\star/R_\odot = (M_\star/{\rm M}_\odot)^{0.8}$. As a result, we have $L_{\rm acc} = (4 \pm 2) \times 10^4 L_\odot$. The uncertainty in $L_{\rm acc}$ corresponds to a stellar mass varying between 10 and 100 $M_\odot$. It is likely that the bolometric luminosity of the dust core ($2.3 \times 10^4\,{\rm L_\odot}$, see Section 4.1) should have a major energy supply from the accretion process.

Considering the existence of the outflow, there should be a strong interaction between the infall and the outflow. And the interaction may be responsible for the 4.5 μm shock emission. Chen et al. (2010) have performed an HCO$^+$ (1 − 0) survey towards the extended green objects (EGOs), i.e. the massive YSO candidates with the 4.5 μm shock emissions. They found that nearly one-third of the sample (29 out of 69 sources) exhibit a significant blue asymmetry. While in an HCO$^+$ (1 − 0) survey towards 82 massive YSOs selected from the methanol masers, only 12 sources have infall signatures (Purcell et al. 2006), comparing these results, it is likely that the shocks are prone to take place in the YSOs with infall motions. This is theoretically expected, since compared to an interaction between the outflow and quiescent gas, an outflow–infall interaction would more efficiently convert the kinetic energy into heat and radiation.

4.4 The molecular abundances and DCN overabundance

The total column density $N_{\rm T}$(X) and abundance $f({\rm X}) = N_{\rm T}({\rm X})/N({\rm H_2})$ of the C^{18}O, HCN, DCN, H^{13}CO$^+$ and C^{34}S are calculated from their emission lines at the continuum emission peak using equations (2) and (3). And a correction for the optical depth is done using equation (4). To derive the HCN and H^{13}CO$^+$ abundances, we used the $N(H_2)$ value for the SCUBA 450 μm continuum (Table 3). While for the SMA lines, we adopted $N(H_2)$ from the 1.3 mm continuum ($0.95 \times 10^{24}\,{\rm cm^{-2}}$). We also note that $N_{\rm T}$(H^{13}CO$^+$) may be underestimated due to the beam dilution, thus should be regarded as a lower limit. To take into account the temperature uncertainty, we also estimated $N_{\rm T}$(X) at the lower limit of $T_{\rm rot} = 20$ K (suggested by the SED fitting). The $N_{\rm T}$(X) and f(X) values are shown in Table 6.

In the calculation of the HCN, its line profile should be corrected for the self-absorption. We modelled its original line profile using the same method for the ^{12}CO (2 − 1) (Section 4.2). However, since the abundance ratio between DCN and HCN is much more uncertain than [C^{18}O/^{12}CO], we cannot use DCN to reliably determine the optical depth of HCN (3 − 2). Nevertheless, we expect the HCN (3 − 2) to have a low optical depth due to two reasons. First, since the HCN (3 − 2) likely traces denser and hotter gas than the ^{12}CO (2 − 1), if the HCN (3 − 2) has a very large optical depth, it should have a comparable intensity with the ^{12}CO (2 − 1). Nevertheless, even after the self-absorption correction, the HCN (3 − 2) is still much weaker than the ^{12}CO (2 − 1). Secondly, with an apparent linewidth ($\Delta V = 6.2\,{\rm km\,s^{-2}}$) being close to ΔV of the C^{18}O and CH_3OH lines (as shown in Table 5), the optical depth broadening should be insignificant for the HCN (3 − 2). We therefore directly calculate $N_{\rm T}$(HCN) and then estimate the optical depth using equation (5). As a result, we found $\tau = 0.78$ at $T_{\rm rot} = 20$ K and 0.10 at 130 K. This result is consistent with our expectation. However, to more accurately determine the HCN optical depth, one should consider observing some other isotopologues such as HC^{15}N (Hatchell, Millar & Rodgers 1998).

From the derived abundances, we can get a relative abundance ratio between DCN and HCN which is [DCN/HCN]$\simeq$ 0.07. The values derived at the two temperature limits are similar to each

Table 6. Column density and abundance of the molecular species.

Molecule (X)	$T_{\rm rot} = 20$ K[a]		$T_{\rm rot} = 130$ K	
	$N_{\rm T}$(X) (cm^{-2})	f(X)	$N_{\rm T}$(X) (cm^{-2})	f(X)
$C^{18}O$	$(2.2 \pm 0.3) \times 10^{16}$	$(2.3 \pm 0.3) \times 10^{-8}$	$(5.4 \pm 0.6) \times 10^{16}$	$(5.6 \pm 0.7) \times 10^{-8}$
CH_3OH[b]	$(1.8 \pm 0.2) \times 10^{15}$	$(2.0 \pm 0.2) \times 10^{-9}$	$(5.3 \pm 0.6) \times 10^{15}$	$(5.8 \pm 0.6) \times 10^{-9}$
$C^{34}S$	$(2.3 \pm 0.3) \times 10^{13}$	$(2.5 \pm 0.4) \times 10^{-11}$	$(2.6 \pm 0.3) \times 10^{13}$	$(2.9 \pm 0.4) \times 10^{-11}$
$H^{13}CO^+$	$(9.5 \pm 1.0) \times 10^{12}$	$(7.9 \pm 0.7) \times 10^{-12}$	$(1.7 \pm 0.2) \times 10^{13}$	$(1.4 \pm 0.1) \times 10^{-11}$
HCN	$(5.6 \pm 0.5) \times 10^{14}$	$(4.6 \pm 0.3) \times 10^{-10}$	$(1.1 \pm 0.1) \times 10^{15}$	$(8.9 \pm 0.8) \times 10^{-10}$
DCN	$(3.1 \pm 0.1) \times 10^{13}$	$(3.4 \pm 0.2) \times 10^{-11}$	$(5.6 \pm 0.3) \times 10^{13}$	$(6.2 \pm 0.5) \times 10^{-11}$
[DCN/HCN][c]	–	0.07 ± 0.01	–	0.07 ± 0.01

[a] A lower limit as suggested by the dust continuum SED.
[b] At $T_{\rm rot} = 20$ K, $N_{\rm T}(CH_3OH)$ is derived from the $3_{-2} - 4_{-1}$ line.
[c] Abundance ratio between DCN and HCN.

other (Table 6). Compared to the cosmic [D/H] ratio (10^{-5}, Linsky 1998), the [DCN/HCN] in G8.68 implies a deuteration for orders of magnitudes. The [DCN/HCN] in G8.68 is also much higher than the values detected in hot molecular cores (10^{-4} to 10^{-3}; Hatchell et al. 1998). However, it is much more comparable to the abundance ratio of [N_2D^+/N_2H^+] detected in high-mass YSOs in the infrared dark clouds (Chen et al. 2011). Overabundant DCN was previously detected in a number of low-mass YSOs (Roberts et al. 2002), while in high-mass star-forming regions, the DCN is not frequently detected.

The overabundant DCN in G8.68 may originate from a high level of deuterium fractionation in the previous cold pre-stellar phase. In highly deuterated gas (abundant in H_2D^+, CH_2D^+, C_2HD^+ etc.), DCN can be produced via D-H substitution of the HCN or through more complex reaction pathways (Albertsson, Semenov & Henning 2011, reactions 17 to 21 therein). Finally, the DCN molecules would mostly reside on the grain mantles (Hatchell et al. 1998; Roberts et al. 2002). During the star formation, the DCN can be released into the gas-phase again. However, once the temperature slightly increases, the gas-phase DCN can be easily destroyed via reactions such as H + DCN → HCN + D (Charnley, Tielens & Millar 1992; Roberts et al. 2002, fig. 5 therein). In this sense, to maintain the DCN overabundance in the gas, two conditions may have to be satisfied. First, there should be a high-level deuterium fractionation in the previous dark-cloud phase. Secondly, in order to compensate the chemical destruction due to the stellar heating, a rapid sublimation for the dust grains should be necessary. Again, the outflow and shocks may have a potential contribution to this process. However, unlike the $C^{34}S$ and CH_3OH, the DCN emission has a compact and spherical morphology which is not evidently coherent with the outflow. Therefore, it is possible that the DCN enhancement is less affected by the shocks and/or more sensitive to the stellar heating. A higher sensitivity and spatial resolution may help better reveal the DCN morphology and determine whether it is associated with the outflow.

As another possibility, the DCN can also be synthesized in the recent gas phase chemistry. Parise et al. (2009) show that the gas-phase reactions may sufficiently account for the enhanced D-H ratio in the molecular gas in the Orion Bar photo-dissociation region (PDR) , which has a [DCN/HCN] ratio of 10^{-2}, comparable with that in G8.68. However, the gas-phase enhancement may have to proceed in an environment with stable lukewarm heating. This condition may hardly be satisfied in regions with a rapid evolution of the high-mass stars. Therefore, the grain mantle sublimation may still be the major process for the DCN enhancement in G8.68. In the future study, one can compare other chemical products from the grain sublimation and gas-phase chemistry in order to determine the relative importance of these two processes.

The $C^{34}S$ abundance in G8.68 is much lower than the average $C^{34}S$ abundance in the UC HII regions (Olmi & Cesaroni 1999). $f(C^{18}O)$ is also much smaller than the typical interstellar medium (ISM) value (1.7×10^{-7}; Frerking, Langer & Wilson 1982). Compared to the ISM abundance, it has a depletion factor of $f_{\rm D}(C^{18}O) = 5 \pm 2$.

5 SUMMARY

We investigated the dust continuum and molecular line emissions towards the high-mass YSO G8.68−0.37. We revealed a dense compact gas-and-dust core in the SMA 1.3 mm continuum emission and its more extended envelope in the SCUBA 450 μm emission. At our angular resolution (spatial scale >0.05 pc), there is no evident fragmentation structures. We find that an SED with at least two temperature components is necessary to account for the dust continuum emissions from mid-infrared to submillimetre wavelengths. The best-fitting temperatures for the two components are $T_{\rm d} = 20$ and 120 K, respectively. The core mass and luminosity are mainly contributed by the cold component ($T_{\rm d} = 20$ K).

Prominent infall signatures and outflow wings are detected in both ^{12}CO (1 − 0) and (2 − 1) lines. We separated the outflow and dense-core components and measured their line parameters. The ^{12}CO (2 − 1) yields an infall velocity of 0.45 km s^{-1}. Assuming that the extended envelope is collapsing towards the inner dense region, we can derive an infall rate of 7×10^{-4} $M_\odot$ yr^{-1}. It is possible that the 4.5 μm shock emission is largely enhanced by a strong interaction between the infall and outflow motions. In addition, we also suggest that the infall motion may be important for suppressing the stellar emissions, thereby protecting the DCN and other fragile species.

We estimated a rotational temperature of 130 K from the CH_3OH lines. We derived the abundances of the molecular species from their spectra, and in particular, we found a high abundance ratio of [DCN/HCN] = 0.07. The over abundant DCN may originate from a high level of deuterium fractionation in the previous pre-protostellar phase, as well as the recent grain mantle sublimation and/or gas-phase chemistry. More details about this chemical process should still be further investigated.

ACKNOWLEDGMENTS

We are grateful to the SMA observers and the SMA data archive. We would thank the anonymous reviewer for the detailed, thoughtful

comments and suggestions helping us to largely improve the presentation and interpretation. This work is supported by the NSFC grant nos 10733033, 10873019 and 10973003, and the NKBRP grant nos 2009CB24901 and 2012CB821800, and the Doctoral Candidate lnnovation Research Support Program (Kjdb 201001-1) from *Science & Technology Review*.

REFERENCES

Albertsson T., Semenov D., Henning Th., 2011, preprint (arXiv: 1110.2644)
Benjamin R. A. et al., 2003, PASP, 115, 953
Beuther H., Schilke P., Menten K. M., Motte F., Sridharan T. K., Wyrowski F., 2002, ApJ, 566, 945
Charnley S. B., Tielens A. G. G. M., Millar T. J., 1992, ApJ, 399, L71
Chen X., Shen Z-Q., Li J-J., Xu Y., He, J-H., 2010, ApJ, 710, 150
Chen H.-R., Liu S.-Y., Su Y.-N., Wang M.-Y., 2011, ApJ, 743, 196
Frerking M. A., Langer W. D., Wilson R. W., 1982, ApJ, 262, 590
Fuller G. A., Williams S. J., Sridharan T. K., 2005, A&A, 442, 949
Garden P. R., Hayashi M., Hasegawa T., Gatley I., Kaifu N., 1991, ApJ, 374, 540
Gong H., Ostrike E. C., 2009, ApJ, 699, 230
Hatchell J., Millar T., Rodgers S., 1998, A&A, 332, 695
Jijina J., Adams F. C., 1996, ApJ, 462, 874
Keto E., 2003, ApJ, 599, 1196
Klaassen P. D., Wilson C. D., 2007, ApJ, 663, 1092
Linsky J. L., 1998, Space Sci. Rev., 84, 285
Longmore S. N., Pillai T., Keto E., Zhang Q., Qiu K., 2011, ApJ, 726, 97 (L11)
Mardones D., Myers P. C., Tafalla M., Wilner D. J., Bachiller R., Garay G., 1997, ApJ, 489, 719
Mueller K., Shirley Y. L., Evans N. J., II, Jacobson H. R., 2002, ApJS, 143, 469
Myers P. C., Mardones D., Tafalla M., Williams J. P., Wilner D. J., 1996, ApJ, 465, L133
Omi L., Cesaroni R., 1999, A&A, 352, 266
Ossenkopf V., Henning T., 1994, A&A, 291, 943
Parise B., Leurini S., Schilke P., Roueff E., Thorwirth S., Lis D. C., 2009, A&A, 508, 737
Pavlyuchenkov Y., Wiebe D., Schustov B., Henning T., Launhardt R., Semenov D., 2008, ApJ, 689, 335
Purcell C. R. et al., 2006, MNRAS, 367, 553
Remijan A., Sutton E. C., Snyder L. E., Friedel D. N., Liu S.-Y., Pei C.-C., 2004, ApJ, 606, 917
Roberts H., Fuller G. A., Millar T. J., Hatchell J., Buckle J. V., 2002, A&A, 381, 1026
Schnee S., Kauffmann J., Goodman A., Bertoldi F., 2007, ApJ, 657, 838
Sollins P. K., Ho P. T. P., 2005, ApJ, 630, 987
Tielens A. G. G. M., 2005, The Physics and Chemistry of the Interstellar Medium. Cambridge Univ. Press, Cambridge
Townes C. H., Schawlow A. L., 1955, Microwave Spectroscopy. McGraw-Hill, New York
Walsh A. J., Burton M. G., Hyland A. R., Robinson G., 1998, MNRAS, 301, 640
Wu J., Evans N. J., II, 2003, ApJ, 592, L79
Wu Y., Wei Y., Zhao M., Shi Y., Yu W., Qin S., Huang M., 2004, A&A, 426, 503
Wu Y., Henkel C., Xue R., Guan X., Miller M., 2007, ApJ, 669, L37
Wyrowski F., Heyminck S., Güsten R., Menten K. M., 2006, A&A, 454, L95
Yorke H. W., Sonnhalter C., 2002, ApJ, 569, 846
Zhang Q., Sridharan T. K., Hunter T. R., Chen Y., Beuther H., Wyrowski F., 2007, A&A, 470, 269
Zhou S., Evans N. J., II, Koempe C., Walmsley C. M., 2009, ApJ, 404, 232

This paper has been typeset from a TEX/LATEX file prepared by the author.